



Cite this: *Phys. Chem. Chem. Phys.*, 2017, 19, 27025

Structural transition in metal-centered boron clusters: from tubular molecular rotors Ta@B₂₁ and Ta@B₂₂⁺ to cage-like endohedral metalloborospherene Ta@B₂₂^{-†}

Hai-Ru Li,^a Hui Liu,^a Xin-Xin Tian,^a Wen-Yan Zan,^a Yue-Wen Mu,^{ib} Hai-Gang Lu,^a Jun Li,^{ib}*^b Yue-Kui Wang*^a and Si-Dian Li^{ib}*^a

Inspired by the recent discovery of the metal-centered tubular molecular rotor C_s B₂-Ta@B₁₈⁻ with the record coordination number of CN = 20 and based on extensive first-principles theory calculations, we present herein the possibility of the largest tubular molecular rotors C_s B₃-Ta@B₁₈ (**1**) and C_{3v} B₄-Ta@B₁₈⁺ (**2**) and smallest axially chiral endohedral metalloborospherenes D₂ Ta@B₂₂⁻ (**3** and **3'**), unveiling a tubular-to-cage-like structural transition in metal-centered boron clusters at Ta@B₂₂⁻ via effective spherical coordination interactions. The highly stable Ta@B₂₂⁻ (**3**) as an elegant superatom, which features two equivalent corner-sharing B₁₀ boron double chains interconnected by two B₂ units with four equivalent B₇ heptagons evenly distributed on the cage surface, conforms to the 18-electron configuration with a bonding pattern of σ + π double delocalization and follows the 2(*n* + 1)² electron counting rule for spherical aromaticity (*n* = 2). Its calculated adiabatic detachment energy of ADE = 3.88 eV represents the electron affinity of the cage-like neutral D₂ Ta@B₂₂ which can be viewed as a superhalogen. The infrared, Raman, VCD, and UV-vis spectra of the concerned species are computationally simulated to facilitate their spectral characterizations.

Received 31st July 2017,
Accepted 12th September 2017

DOI: 10.1039/c7cp05179d

rsc.li/pccp

1. Introduction

As a prototypical electron-deficient element dominated by multicenter-two-electron bonds (mc-2e bonds) in both bulk allotropes and polyhedral molecules, boron has a rich chemistry next only to carbon in the periodic table. A systematical joint photoelectron spectroscopy (PES) and first-principles theory (FPT) investigation performed in the past decade on small boron monoanions has revealed a rich landscape from planar or quasi-planar B_{*n*}⁻⁰ sheets (*n* = 3–30, 35–38) to cage-like borospherenes D_{2d} B₄₀⁻⁰ and C₃/C₂ B₃₉⁻¹⁻¹⁴ with seashell-like C₂ B₂₈⁻¹³ and C_s B₂₉⁻⁹ coexisting as minor isomers in gas phases. Endohedral metalloborospherenes M@B₄₀ (M = Ca, Sr, Sc, Y, La)^{15,16} were subsequently predicted to be viable species at FPT levels. In the past two years, our group has extended the borospherene family at FPT levels to include cage-like B₄₁^{+/B₄₂²⁺},¹⁷ B₄₀⁺,¹⁸ B₃₉⁺,¹⁹ B₃₈²⁻ (in Ca@B₃₈),²⁰ B₃₇³⁻ (in Ca@B₃₇⁻),²¹ and B₃₆⁴⁻ (in Li₄@B₃₆),²² which are all

composed of twelve interwoven boron double chains (BDCs) with six hexagonal or heptagonal faces and follow the universal bonding pattern of σ + π double delocalization. Ion-mobility measurements, on the other hand, showed that double-ring tubular B_{*n*}⁺ monocations start to appear at *n* = 16,²³ revealing another important structural domain in boron clusters. The latest breakthrough in boron nanostructures was the successful syntheses of monolayer borospherenes on the Ag(111) substrate among which the most stable χ³-borophene consists of zigzag BDCs alternated with rows of adjacent hexagonal holes.^{24,25} Stable BDCs were previously reported in elongated B_{*n*}H₂^{-2/-1/0} clusters up to *n* = 22,²⁶⁻²⁸ laying the foundation for the double-chain chemistry of boron.

Transition-metal dopants can dramatically change the geometrical and electronic structures of small boron clusters and lead to earlier 2D to 3D transitions in metal-doped boron clusters via effective coordination interactions. A series of perfect planar metal-centered boron wheels including D_{8h} Co@B₈⁻, D_{9h} Rh@B₉⁻, and D_{10h} Ta@B₁₀⁻ with the maximum coordination number of CN = 10 in planar species were characterized in the gas phase,²⁹⁻³¹ while CoB₁₂⁻ and RhB₁₂⁻ with a quasi-planar B₁₂ ligand analogous to benzene were found to adopt half-sandwich structures.³² For larger MB_{*n*}⁻ monoanions, PES measurements in combination with FPT calculations

^a Institute of Molecular Science, Shanxi University, Taiyuan, 030006, China.
E-mail: lisidian@sxu.edu.cn, ykwang@sxu.edu.cn

^b Department of Chemistry, Tsinghua University, Beijing 100084, China.
E-mail: junli@mail.tsinghua.edu.cn

† Electronic supplementary information (ESI) available. See DOI: 10.1039/c7cp05179d

confirmed that D_{8d} CoB_{16}^- , D_{8d} MnB_{16}^- , and D_{9d} RhB_{18}^- possess perfect metal-centered drum-like structures *via* effective tubular coordination interactions with CN = 16, 16, and 18, respectively,^{33–35} while C_{2v} CoB_{18}^- proved to be a perfectly planar borophene-type cluster due to the truncated Co 3d orbitals.³⁶ Metal-centered drum-like $\text{M}@B_{2n}$ ($\text{M} = \text{Ti}, \text{Cr}, \text{Fe}, \text{Ni}, \text{Zn}; n = 6, 7, 8$) were also predicted in theory.³⁷ The first tubular molecular rotor C_s $\text{B}_2\text{-Ta}@B_{18}^-$ and perfect drum-like D_{10d} $\text{Ta}@B_{20}^-$ with the record coordination number of CN = 20 were recently discovered in PES measurements in combination with FPT calculations.³⁸ It is natural to ask at the current stage what is the upper limit in cluster size to form tubular molecular rotors and when cage-like endohedral structures start to dominate in thermodynamics in metal-centered MB_n boron clusters? Metal-encapsulated cage-like D_{3h} $\text{M}@B_{24}$ clusters ($\text{M} = \text{Mo}$ and W) were previously proposed at FPT.³⁹ However, to the best of our knowledge, the smallest cage-like metal-centered boron cluster in this size range at which the tubular-to-cage-like structural transition occurs still remains unknown in both theory and experiments.

Based on extensive global-minimum search and FPT calculations, we predict in this work the possible existence of the largest tubular molecular rotors C_s $\text{B}_3\text{-Ta}@B_{18}$ (**1**) and C_{3v} $\text{B}_4\text{-Ta}@B_{18}^+$ (**2**) and smallest axially chiral endohedral metalloborospherenes D_2 $\text{Ta}@B_{22}^-$ (**3** and **3'**), revealing a tubular-to-cage-like structural transition in metal-centered boron clusters *via* effective spherical coordination interactions at $\text{Ta}@B_{22}^-$ with CN = 22. While $\text{B}_4\text{-Ta}@B_{18}^+$ (**2**) possesses a B_4 pyramid rotating almost freely atop the $\text{Ta}@B_{18}$ drum at finite temperatures, the highly stable cage-like $\text{Ta}@B_{22}^-$ (**3/3'**) clusters featuring two equivalent corner-sharing B_{10} BDCs interconnected by two B_2 units with four equivalent B_7 heptagons on the surface conform to the 18 electron rule with a $\sigma + \pi$ double delocalization bonding pattern. These stable metal-centered boron complexes and their isoivalent species may serve as building blocks to form novel boron-based nanomaterials.

2. Computational methods

Extensive unbiased global-minimum searches were performed on TaB_{21} , TaB_{22}^+ , and TaB_{22}^- using both the Minima Hopping (MH) algorithm^{40,41} and the TGmin code⁴² at the PBE level,⁴³ in combination with manual structural constructions based on the known structures of B_{20}^- , TaB_{20}^- , B_{21}^- , and B_{22}^- . Low-lying structures were then fully optimized at both the hybrid PBE0⁴⁴ and TPSSh⁴⁵ levels implemented in the Gaussian 09 program,⁴⁶ using the 6-311+G*⁴⁷ basis set for B and the Stuttgart ECP basis set^{48,49} for Ta. Single-point energies were further refined for the twelve lowest-lying isomers at the more accurate CCSD(T)/B/6-311G*/Ta/Stuttgart level^{50–52} at PBE0 geometries, using the MOLPRO package.⁵³ Chemical bonding analyses were performed using the adaptive natural density partitioning (AdNDP) method.⁵⁴ Natural bonding orbital analyses were performed using the NBO 6.0 program.⁵⁵ Molecular dynamics (MD) simulations were done on $\text{B}_4\text{-Ta}@B_{18}^+$ (**2**) and $\text{Ta}@B_{22}^-$ (**3**) for 30 ps using the CP2K software suite.⁵⁶ UV-vis spectra were simulated using the time-dependent approach⁵⁷ at PBE0.

3. Results and discussion

3.1. Structures and stabilities

We start from the tubular neutral C_s $\text{B}_3\text{-Ta}@B_{18}$ (**1**, $^1A'$) which can be obtained by inserting a B^+ atom into the B_2 unit in the experimentally known C_s $\text{B}_2\text{-Ta}@B_{18}^-$,³⁸ with a V-shaped B_3 bridge ($\equiv\text{B-B-B}\equiv$) atop the $\text{Ta}@B_{18}$ drum with a B_6 hexagon and a B_7 heptagon on two sides (Fig. 1). Encouragingly, with over 2260 stationary points probed on the potential energy surface, $\text{B}_3\text{-Ta}@B_{18}$ (**1**) turns out to be the global minimum (GM) of the system (Fig. S1a, ESI[†]) with the large HOMO–LUMO gap of $\Delta E_{\text{gap}} = 2.64$ eV (Fig. S2a, ESI[†]). It lies 0.14 eV lower than the second isomer C_s $\text{B}_3\text{-Ta}@B_{18}$ ($^1A'$) which also possesses a B_3 unit ($\equiv\text{B-B-B}\equiv$) atop the $\text{Ta}@B_{18}$ drum with a B_8 octagon and a B_5 pentagon on two sides at the CCSD(T) level. The third isomer C_s $\text{B}_3\text{-Ta}@B_{18}$ with a B_3 chain ($-\text{B-B-B}-$) over a buckled $\text{Ta}@B_{18}$ drum lies 0.15 eV higher than the GM. Other low-lying 3D isomers lie at least 0.18 eV higher than the GM. $\text{B}_3\text{-Ta}@B_{18}$ (**1**) with the average Ta–B distance of 2.47 Å is thus the second tubular molecular rotor reported after $\text{B}_2\text{-Ta}@B_{18}^-$ ³⁸ with CN = 21.

With the addition of one more B^+ , the high-symmetry tubular C_{3v} $\text{B}_4\text{-Ta}@B_{18}^+$ (**2**, 1A_1) is achieved which contains a B_4 pyramid atop a $\text{Ta}@B_{18}$ drum with three equivalent B_5 pentagons evenly distributed around the C_3 molecular axis. More encouragingly, with more than 3300 stationary points explored, $\text{B}_4\text{-Ta}@B_{18}^+$ (**2**) with $\Delta E_{\text{gap}} = 2.29$ eV (Fig. S2, ESI[†]) turns out to be the GM of the monocation, as shown in its configurational energy spectrum in Fig. 2a at CCSD(T). The second lowest-lying isomer C_1 $\text{B}_4\text{-Ta}@B_{18}^+$ which is slightly distorted from a perfect C_{3v} $\text{B}_4\text{-Ta}@B_{18}^+$ with three equivalent B_6 hexagons atop the $\text{Ta}@B_{18}$ drum possesses a small relative energy of +0.08 eV at CCSD(T). It is expected to coexist with the GM in the gas phase. The third lowest-lying isomer C_1 $\text{B}_4\text{-Ta}@B_{18}^+$ with a distorted B_4 unit atop a buckled $\text{Ta}@B_{18}$ drum lies 0.27 eV higher than **2**. All the other tubular or cage-like isomers appear to be at least 0.40 eV less stable than the GM. $\text{B}_4\text{-Ta}@B_{18}^+$ (**2**) with the average Ta–B distance of 2.48 Å is thus the third and largest tubular molecular rotor reported to date with CN = 22. It is noticed that all the stable tubular molecular rotors C_s $\text{B}_2\text{-Ta}@B_{18}^-$,³⁸ C_s $\text{B}_3\text{-Ta}@B_{18}$ (**1**), and C_{3v} $\text{B}_4\text{-Ta}@B_{18}^+$ (**2**) contain a robust $\text{Ta}@B_{18}$ drum at the bottom as the structural basis. Tubular neutral C_{3v} $\text{B}_4\text{-Hf}@B_{18}$ isoivalent with $\text{B}_4\text{-Ta}@B_{18}^+$ (**2**) also appears to be a true minimum of the system.

With one electron attached to $\text{B}_4\text{-Ta}@B_{18}^+$ (**2**), a high-symmetry tubular C_{3v} $\text{B}_4\text{-Ta}@B_{18}$ (2A_2) is generated which is

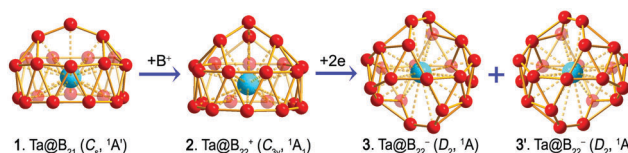


Fig. 1 Optimized structures of the largest tubular molecular rotors C_s $\text{B}_3\text{-Ta}@B_{18}$ (**1**) and C_{3v} $\text{B}_4\text{-Ta}@B_{18}^+$ (**2**) and the smallest axially chiral endohedral metalloborospherene D_2 $\text{Ta}@B_{22}^-$ (**3**) and its degenerate enantiomer D_2 $\text{Ta}@B_{22}^-$ (**3'**) at the PBE0 level. Dashed lines represent Ta–B coordination interactions.

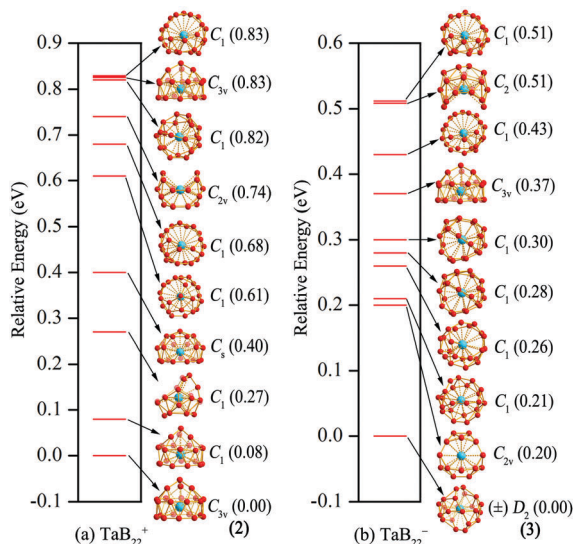


Fig. 2 Configurational energy spectra of (a) TaB_{22}^+ and (b) TaB_{22}^- with energies relative to the global minima indicated in eV at the CCSD(T) level.

the lowest-lying isomer of neutral TaB_{22} (Fig. S1c, ESI[†]). However, attachment of an extra electron leads to a dramatic geometrical change in the system to produce the axially chiral endohedral metalloborospherene $D_2 \text{Ta@B}_{22}^-$ (**3**, 1A) and its degenerate enantiomer $D_2 \text{Ta@B}_{22}^-$ (**3'**, 1A) (Fig. 1) both of which contain four equivalent B_7 heptagons evenly distributed on the cage surface. Most encouragingly, extensive GM searches with more than 4000 stationary points explored indicate that Ta@B_{22}^- (**3/3'**) are overwhelmingly the GMs of the monoanion (Fig. 2b), which feature two equivalent corner-sharing B_{10} BDCs interconnected by two B_2 units, with two tetracoordinate >B< centers in the front and at the back and two >B-B< bridges on the top and at the bottom. The second lowest-lying sandwich-like $C_{2v} \text{Ta@B}_{22}^-$ with one B_8 ligand on the top and one B_{10} ligand at the bottom interconnected by four equivalent tricoordinate -B< atoms on the waist appears to be 0.20 eV less stable than **3/3'** at CCSD(T) (Fig. 2b). Other low-lying isomers within 0.51 eV are either cage-like or tubular, with the perfect tubular $C_{3v} B_4\text{-Ta@B}_{18}^-$ as the seventh isomer lying 0.37 eV higher than the GMs. Cage-like Ta@B_{22}^- (**3/3'**) clusters with the average Ta–B distance of 2.48 Å are therefore the first and smallest endohedral metalloborospherenes reported to date with CN = 22. Axially chiral $D_2 M@B_{22}^-$ ($M = V, Nb$), $D_2 M@B_{22}$ ($M = Cr, Mo, W$), and $D_2 M@B_{22}^+$ ($M = Mn, Tc, Re$) isovalent with Ta@B_{22}^- (**3/3'**) are all true minima of the systems. The transition-metal centers and the cage-like $\eta^{22}\text{-B}_{22}$ ligand in these endohedral complexes match nicely both geometrically and electronically, forming effective spherical coordination interactions between the metal center and the $D_2 B_{22}$ ligand. Initial investigations show that, similar to Ta@B_{22}^- (**3/3'**), closed-shell TaB_{23} , TaB_{24}^+ , and TaB_{24}^- also favor endohedral cage-like structures with CN ≥ 23 over their planar or tubular rivals.

Extensive molecular dynamics (MD) simulations show that Ta@B_{22}^- (**3**) remains dynamically stable at 800 K, with the small root-mean-square-deviation of RMSD = 0.11 Å and the

maximum bond length deviation of MAXD = 0.34 Å (Fig. S3, ESI[†]). It starts to hop between the two degenerate enantiomers Ta@B_{22}^- (**3**) and Ta@B_{22}^- (**3'**) at 1000 K in concerted mechanisms, with RMSD = 0.19 Å and MAXD = 0.67 Å. In comparison, as shown in the ESI[†] Video, $B_4\text{-Ta@B}_{18}^+$ (**2**) exhibits typical rotational structural fluctuations at 600 K, similar to the situation observed in the first observed tubular molecular rotor $B_2\text{-Ta@B}_{18}^-$.³⁸ The B_4 pyramid in C_{3v} **2** rotates essentially freely atop the Ta@B_{18} drum, with three transition states located (two C_s and one C_1) which lie only 2.00, 1.80, and 1.57 kcal mol⁻¹ above the GM at CCSD(T) (Fig. S4, ESI[†]), respectively. These low-lying transition states can be obtained from a perfect $C_{3v} B_4\text{-Ta@B}_{18}^+$ with three equivalent B_6 hexagons atop the Ta@B_{18} drum in its degenerate e and nondegenerate a₂ imaginary vibrational modes (Fig. S4, ESI[†]).

3.2. Electronic structures and bonding analyses

The high stabilities of $B_3\text{-Ta@B}_{18}^+$ (**1**), $B_4\text{-Ta@B}_{18}^+$ (**2**), and Ta@B_{22}^- (**3/3'**) originate from their unique electronic configurations and bonding patterns. Fig. 3 compares the eigenvalue spectra of the bare $D_2 B_{22}$ ligand and the Ta-centered $D_2 \text{Ta@B}_{22}^-$ (**3**) complex, with nine π orbitals over the cage surface depicted. The HOMO–LUMO energy gap increases dramatically from $\Delta E_{\text{gap}} = 0.84$ eV in $D_2 B_{22}$ to $\Delta E_{\text{gap}} = 3.60$ eV in $D_2 \text{Ta@B}_{22}^-$ (**3**), rendering high chemical stability to the endohedral metalloborospherene. The bare $D_2 B_{22}$ possesses six occupied π -orbitals (HOMO, HOMO–1, 6, 8, 10, and 14) and three unoccupied π -orbitals (LUMO, LUMO+1, LUMO+2). These out-of-surface π -orbitals interact with the valence orbitals of the Ta center ($5d^36s^2$) to form hybridized orbitals in $D_2 \text{Ta@B}_{22}^-$ (**3**). As shown in Fig. 3, Ta@B_{22}^- (**3**) as an elegant superatom possesses nine occupied atomic-like orbitals *via* spd- π interaction/hybridization, *i.e.* HOMO–19 (s), HOMO–13 (p_x), HOMO–12 (p_y),

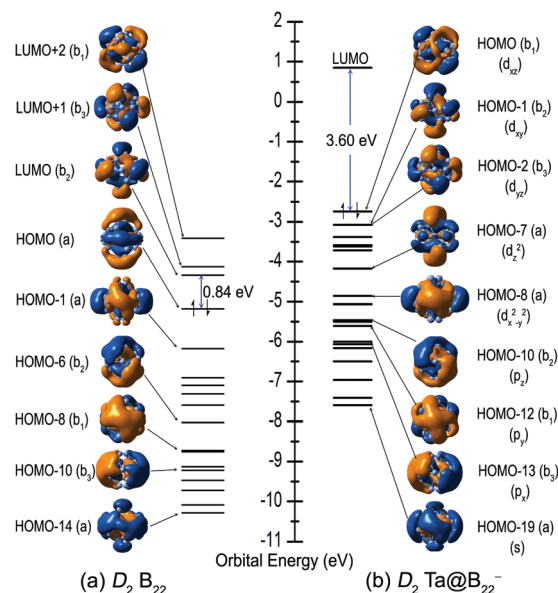


Fig. 3 Eigenvalue spectra of (a) bare $D_2 B_{22}$ and (b) metal-centered $D_2 \text{Ta@B}_{22}^-$ (**3/3'**) with the HOMO–LUMO energy gaps indicated in eV at the PBE0 level. The nine π orbitals over the cage surface involved in the 18-electron configuration are depicted for comparison.

HOMO–10 (p_z), HOMO–8 ($d_{x^2-y^2}$), HOMO–7 (d_{z^2}), HOMO–2 (d_{yz}), HOMO–1 (d_{xy}), and HOMO (d_{xz}). Such an electronic configuration conforms to the 18-electron rule, eliminates the three unoccupied π -orbitals in the D_2 B_{22} cage, and effectively stabilizes the $Ta@B_{22}^-$ (3) complex. With the natural electronic configuration of $Ta[Xe]6s^{0.27}5d^{4.54}$, the Ta centers in $Ta@B_{22}^-$ (3) donates its $6s^2$ electrons almost completely to the B_{22} ligand while, in return, accepts roughly two electrons in its partially filled 5d orbitals from the out-of-surface p_π orbitals of the cage-like η^{22} - B_{22} ligand *via* effective back-donations. The calculated Ta–B bond orders between 0.24 and 0.29 in $Ta@B_{22}^-$ (3) are comparable with the typical Cr–C coordination bond order of 0.34 in D_{6h} $Cr(C_6H_6)_2$ and the Fe–C coordination bond order of 0.30 in D_{5h} $Fe(C_5H_5)_2$. The Ta center in $Ta@B_{22}^-$ (3) has the highest total Wiberg bond order of 5.91, in comparison with the corresponding values of 5.87, 5.74, 5.69, 4.19, and 3.06 calculated for the metal centers in B_4 - $Ta@B_{18}^+$ (2), B_3 - $Ta@B_{18}$ (1), B_2 - $Ta@B_{18}^-$,³⁸ $Cr(C_6H_6)_2$, and $Fe(C_5H_5)_2$, respectively, well supporting the strong spherical coordination interactions between the Ta center and the η^{22} - B_{22} ligand in 3.

Detailed AdNDP analyses indicate that $Ta@B_{22}^-$ (3) possesses 2 $2c-2e$, 20 $3c-2e$, 2 $5c-2e$, 2 $6c-2e$, and 1 $22c-2e$ σ bonds on the D_2 B_{22} cage surface (Fig. S5, ESI†). Over the σ -skeleton, there exist nine delocalized π bonds involving the Ta center which correspond to the nine occupied π -orbitals shown in Fig. 3, including two equivalent $6c-2e$ π bonds in the y -direction over the two tetracoordinate $>B<$ centers in the front and at the back, two equivalent $7c-2e$ π bonds in the z -direction over the two $>B-B<$ bridges on the top and at the bottom, two equivalent $9c-2e$ π bonds in the x -direction over the two remaining B_8 BDCs on the right and left, and three $23c-2e$ totally delocalized π bonds over the whole B_{22} cage. $Ta@B_{22}^-$ (3) thus follows the bonding pattern of $\sigma + \pi$ double delocalization which was firstly observed in the borospherene family.^{4,5,17–22} Such a bonding pattern conforms to the $2(n+1)^2$ electron counting rule for spherical aromaticity ($n = 2$) and provides extra stability to the metal-centered cage-like boron complex, as evidenced by the fact that the calculated HOMO–LUMO gap of 3.60 eV in $Ta@B_{22}^-$ (3) is even higher than the corresponding values of 3.02 eV and 3.13 eV in C_{60} and B_{40} at the same theoretical level, respectively.⁴ In fact, the closed-shell $Ta@B_{22}^-$ (3) possesses a relatively high first vertical detachment energy of VDE = 4.05 eV at CCSD(T) in the metal-doped boron cluster series.^{29–36,38} Its calculated adiabatic detachment energy of ADE = 3.88 eV corresponds to the electron affinity of the cage-like neutral D_2 $Ta@B_{22}$, which can be viewed as a superhalogen.

The eigenvalue spectrum of B_4 - $Ta@B_{18}^+$ (2) shown in Fig. S2b (ESI†) indicates that the B_4 pyramidal unit is effectively stabilized by the coordination interactions in the vertical direction between the B_4 p_π and Ta $5d_{z^2}$, $5d_{xz}$, and $5d_{yz}$ in the HOMO (a_1) and degenerate HOMO–1 (e). The Ta–B bond orders (0.32–0.35) involving the B_4 pyramid cap are indeed much higher than that (0.24–0.27) involving the B_{18} drum in B_4 - $Ta@B_{18}^+$ (2). Similar coordination interactions exist in both B_3 - $Ta@B_{18}$ (1) (Fig. S2a, ESI†) and the experimentally observed B_2 - $Ta@B_{18}^-$.³⁸

3.3. Simulated IR, Raman, VCD, and UV-vis spectra

We computationally simulate the infrared (IR), Raman, vibrational circular dichroism (VCD), and UV-vis spectra of D_2 $Ta@B_{22}^-$ (3) in Fig. 4 and the related spectra of C_s B_3 - $Ta@B_{18}$ (1), C_{3v} B_4 - $Ta@B_{18}^+$ (2), and the second lowest-lying C_1 B_4 - $Ta@B_{18}^+$ in Fig. S6–S8 (ESI†) to facilitate their spectral characterizations. Infrared photodissociation (IR-PD) spectral measurements have proven to be a powerful means to characterize novel clusters in gas phases.⁵⁸ As shown in Fig. 4a, $Ta@B_{22}^-$ (3) possesses six major IR peaks at 265 ($2b_2$), 404 ($5b_2$), 619 ($9b_3$), 784 ($11b_2$), 945 ($13b_2$), and 1081 ($14b_2$) cm^{-1} , respectively. The strongest Raman peak at 664 cm^{-1} (10a) (Fig. 4b) corresponds to a typical radial breathing mode which may be used to characterize its cage-like structure.⁵⁹ Its VCD spectrum involves 47 vibrational transitions of fundamental frequency (Fig. 4c and Table S1, ESI†), including 15 transitions of $0 \rightarrow b_1$, 16 of $0 \rightarrow b_2$, and 16 of $0 \rightarrow b_3$ which are all electric and magnetic dipole allowed. Five of the normal vibration modes, *i.e.*, $11b_2$, $12b_1$, $14b_1$, $16b_3$, and $16b_2$, yield strong VCD absorption bands which could be used to identify $Ta@B_{22}^-$ (3) in the gas phase. In particular, $11b_2$, the most negative VCD signal at 784 cm^{-1} , represents the VCD spectral characteristics of the axially chiral $Ta@B_{22}^-$ (3). The strong UV features of $Ta@B_{22}^-$ (3) (Fig. 4d) below 300 nm originate from electron transitions from the deep inner shells to the high-lying unoccupied molecular orbitals of the monoanion, while the weak absorption bands above 450 nm mainly involve electron transitions from the HOMO and HOMO–1 of the systems. $Ta@B_{22}^-$ (3') as an enantiomer has the same IR, Raman, and UV-vis spectra as $Ta@B_{22}^-$ (3), but its VCD is a mirror of the latter with opposite signs (Fig. S9, ESI†).

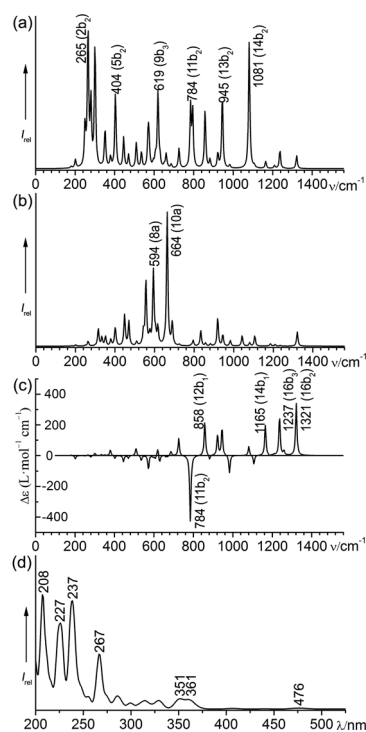


Fig. 4 Computationally simulated (a) IR, (b) Raman, (c) VCD, and (d) UV-vis spectra of D_2 $Ta@B_{22}^-$ (3) at the PBE0 level.

4. Conclusions

In summary, we have predicted a tubular-to-cage-like structural transition in metal-centered boron clusters at the smallest spherically aromatic endohedral metalloborospherenes D_2 Ta@B₂₂⁻ (3/3') which, as elegant superatoms, conform to the 18 electron rule with the bonding pattern of $\sigma + \pi$ double delocalization. Preliminary investigations indicate that the four equivalent B₇ heptagons on the cage surface of 3/3' may serve as effective η^7 -B₇ ligands to coordinate various transition metal centers like Ni, Pd, and Pt to form endohedral heteroborospherenes. C_{3v} B₄-Ta@B₁₈⁺ (2), D_2 Ta@B₂₂⁻ (3/3'), and their neutral isovalent counterparts C_{3v} B₄-Hf@B₁₈ and D_2 W@B₂₂ are possible molecular devices to form novel complexes and cluster-assembled nanomaterials.

Conflicts of interest

There are no conflicts to declare.

Acknowledgements

This project was financially supported by the National Natural Science Foundation of China (21720102006, 21590792, 21373130, 11504213, and 21473106).

Notes and references

- L. S. Wang, *Int. Rev. Phys. Chem.*, 2016, **35**, 69–142.
- A. N. Alexandrova, A. I. Boldyrev, H. J. Zhai and L. S. Wang, *Coord. Chem. Rev.*, 2006, **250**, 2811–2866.
- A. P. Sergeeva, I. A. Popov, Z. A. Piazza, W. L. Li, C. Romanescu, L. S. Wang and A. I. Boldyrev, *Acc. Chem. Res.*, 2014, **47**, 1349–1358.
- H. J. Zhai, Y. F. Zhao, W. L. Li, Q. Chen, H. Bai, H. S. Hu, Z. A. Piazza, W. J. Tian, H. G. Lu, Y. B. Wu, Y. W. Mu, G. F. Wei, Z. P. Liu, J. Li, S. D. Li and L. S. Wang, *Nat. Chem.*, 2014, **6**, 727–731.
- Q. Chen, W. L. Li, Y. F. Zhao, S. Y. Zhang, H. S. Hu, H. Bai, H. R. Li, W. J. Tian, H. G. Lu, H. J. Zhai, S. D. Li, J. Li and L. S. Wang, *ACS Nano*, 2015, **9**, 754–760.
- A. P. Sergeeva, D. Y. Zubarev, H. J. Zhai, A. I. Boldyrev and L. S. Wang, *J. Am. Chem. Soc.*, 2008, **130**, 7244–7246.
- W. Huang, A. P. Sergeeva, H. J. Zhai, B. B. Averkiev, L. S. Wang and A. I. Boldyrev, *Nat. Chem.*, 2010, **2**, 202–206.
- W. L. Li, R. Pal, Z. A. Piazza, X. C. Zeng and L. S. Wang, *J. Chem. Phys.*, 2015, **142**, 204305.
- H. R. Li, T. Jian, W. L. Li, C. Q. Miao, Y. J. Wang, Q. Chen, X. M. Luo, K. Wang, H. J. Zhai, S. D. Li and L. S. Wang, *Phys. Chem. Chem. Phys.*, 2016, **18**, 29147–29155.
- W. L. Li, Y. F. Zhao, H. S. Hu, J. Li and L. S. Wang, *Angew. Chem., Int. Ed.*, 2014, **53**, 5540–5545.
- W. L. Li, Q. Chen, W. J. Tian, H. Bai, Y. F. Zhao, H. S. Hu, J. Li, H. J. Zhai, S. D. Li and L. S. Wang, *J. Am. Chem. Soc.*, 2014, **136**, 12257–12260.
- Z. A. Piazza, H. S. Hu, W. L. Li, Y. F. Zhao, J. Li and L. S. Wang, *Nat. Commun.*, 2014, **5**, 3113.
- Y. J. Wang, Y. F. Zhao, W. L. Li, T. Jian, Q. Chen, X. R. You, T. Ou, X. Y. Zhao, H. J. Zhai, S. D. Li, J. Li and L. S. Wang, *J. Chem. Phys.*, 2016, **144**, 064307.
- Q. Chen, W. J. Tian, L. Y. Feng, H. G. Lu, Y. W. Mu, H. J. Zhai, S. D. Li and L. S. Wang, *Nanoscale*, 2017, **9**, 4550–4557.
- H. Bai, Q. Chen, H. J. Zhai and S. D. Li, *Angew. Chem., Int. Ed.*, 2015, **54**, 941–945.
- P. Jin, Q. Hou, C. Tang and Z. Chen, *Theor. Chem. Acc.*, 2015, **134**, 13.
- G. D. Purvis and R. J. Bartlett, *J. Chem. Phys.*, 1982, **76**, 1910–1918.
- H. R. Li, Q. Chen, X. X. Tian, H. G. Lu, H. J. Zhai and S. D. Li, *J. Mol. Model.*, 2016, **22**, 124.
- X. Y. Zhao, Q. Chen, H. R. Li, Y. W. Mu, H. G. Lu and S. D. Li, *Phys. Chem. Chem. Phys.*, 2017, **19**, 10998–11003.
- Q. Chen, H. R. Li, C. Q. Miao, Y. J. Wang, H. G. Lu, Y. W. Mu, G. M. Ren, H. J. Zhai and S. D. Li, *Phys. Chem. Chem. Phys.*, 2016, **18**, 11610–11615.
- Q. Chen, H. R. Li, W. J. Tian, H. G. Lu, H. J. Zhai and S. D. Li, *Phys. Chem. Chem. Phys.*, 2016, **18**, 14186–14190.
- W. J. Tian, Q. Chen, H. R. Li, M. Yan, Y. W. Mu, H. G. Lu, H. J. Zhai and S. D. Li, *Phys. Chem. Chem. Phys.*, 2016, **18**, 9922–9926.
- E. Oger, N. R. Crawford, R. Kelting, P. Weis, M. M. Kappes and R. Ahlrichs, *Angew. Chem., Int. Ed.*, 2007, **46**, 8503–8506.
- A. J. Mannix, X. F. Zhou, B. Kiraly, J. D. Wood, D. Alducin, B. D. Myers, X. L. Liu, B. L. Fisher, U. Santiago, J. R. Guest, M. J. Yacaman, A. Ponce, A. R. Oganov, M. C. Hersam and N. P. Guisinger, *Science*, 2015, **350**, 1513–1516.
- B. Feng, J. Zhang, Q. Zhong, W. Li, S. Li, H. Li, P. Cheng, S. Meng, L. Chen and K. Wu, *Nat. Chem.*, 2016, **8**, 563–568.
- D. Z. Li, Q. Chen, Y. B. Wu, H. G. Lu and S. D. Li, *Phys. Chem. Chem. Phys.*, 2012, **14**, 14769–14774.
- W. L. Li, C. Romanescu, T. Jian and L. S. Wang, *J. Am. Chem. Soc.*, 2012, **134**, 13228–13231.
- H. Bai, H. J. Zhai, S. D. Li and L. S. Wang, *Phys. Chem. Chem. Phys.*, 2013, **15**, 9646–9653.
- C. Romanescu, T. R. Galeev, W. L. Li, A. I. Boldyrev and L. S. Wang, *Acc. Chem. Res.*, 2013, **46**, 350–358.
- T. R. Galeev, C. Romanescu, W. L. Li, L. S. Wang and A. I. Boldyrev, *Angew. Chem., Int. Ed.*, 2012, **51**, 2101–2105.
- W. L. Li, C. Romanescu, T. R. Galeev, Z. A. Piazza, A. I. Boldyrev and L. S. Wang, *J. Am. Chem. Soc.*, 2012, **134**, 165–168.
- I. A. Popov, W. L. Li, Z. A. Piazza, A. I. Boldyrev and L. S. Wang, *J. Phys. Chem. A*, 2014, **118**, 8098–8105.
- I. A. Popov, T. Jian, G. V. Lopez, A. I. Boldyrev and L. S. Wang, *Nat. Commun.*, 2015, **6**, 8654.
- T. Jian, W. L. Li, I. A. Popov, G. V. Lopez, X. Chen, A. I. Boldyrev, J. Li and L. S. Wang, *J. Chem. Phys.*, 2016, **144**, 154310.
- T. Jian, W. L. Li, X. Chen, T. T. Chen, G. V. Lopez, J. Li and L. S. Wang, *Chem. Sci.*, 2016, **7**, 7020–7027.
- W. L. Li, T. Jian, X. Chen, T. T. Chen, G. V. Lopez, J. Li and L. S. Wang, *Angew. Chem., Int. Ed.*, 2016, **55**, 7358–7363.

- 37 C. Xu, L. Cheng and J. Yang, *J. Chem. Phys.*, 2014, **141**, 124301.
- 38 W. L. Li, T. Jian, X. Chen, H. R. Li, T. T. Chen, X. M. Luo, S. D. Li, J. Li and L. S. Wang, *Chem. Commun.*, 2017, **53**, 1587–1590.
- 39 J. Lv, Y. Wang, L. Zhang, H. Lin, J. Zhao and Y. Ma, *Nanoscale*, 2015, **7**, 10482–10489.
- 40 S. Goedecker, *J. Chem. Phys.*, 2004, **120**, 9911–9917.
- 41 S. Goedecker, W. Hellmann and T. Lenosky, *Phys. Rev. Lett.*, 2005, **95**, 055501.
- 42 X. Chen, Y.-F. Zhao, L.-S. Wang and J. Li, *Comput. Theor. Chem.*, 2017, **1107**, 57–65.
- 43 J. P. Perdew, K. Burke and M. Ernzerhof, *Phys. Rev. Lett.*, 1996, **77**, 3865–3868.
- 44 C. Adamo and V. Barone, *J. Chem. Phys.*, 1999, **110**, 6158–6170.
- 45 J. Tao, J. P. Perdew, V. N. Staroverov and G. E. Scuseria, *Phys. Rev. Lett.*, 2003, **91**, 146401.
- 46 R. Krishnan, J. S. Binkley, R. Seeger and J. A. Pople, *J. Chem. Phys.*, 1980, **72**, 650–654.
- 47 D. Feller, *J. Comput. Chem.*, 1996, **17**, 1571–1586.
- 48 D. Feller, *J. Comput. Chem.*, 1996, **17**, 1571–1586.
- 49 K. L. Schuchardt, B. T. Didier, T. Elsethagen, L. S. Sun and V. Gurumoorthi, *J. Chem. Inf. Model.*, 2007, **47**, 1045–1052.
- 50 J. Čížek, *Adv. Chem. Phys.*, 1969, **14**, 35–89.
- 51 G. D. Purvis and R. J. Bartlett, *J. Chem. Phys.*, 1982, **76**, 1910–1918.
- 52 K. Raghavachari, G. W. Trucks, J. A. Pople and M. Head-Gordon, *Chem. Phys. Lett.*, 1989, **157**, 479–483.
- 53 M. J. Frisch, *et al.*, *Gaussian 09, Revision D.01*, Gaussian, Inc., Wallingford, CT, 2009.
- 54 D. Y. Zubarev and A. I. Boldyrev, *Phys. Chem. Chem. Phys.*, 2008, **10**, 5207–5217.
- 55 E. D. Glendening, J. K. Badenhoop, A. E. Reed, J. E. Carpenter, J. A. Bohmann, C. M. Morales, C. R. Landis and F. Weinhold, *NBO 6.0*, Theoretical Chemistry Institute, University of Wisconsin, Madison, 2013.
- 56 J. VandeVondele, M. Krack, F. Mohamed, M. Parrinello, T. Chassaing and J. Hutter, *Comput. Phys. Commun.*, 2005, **167**, 103–128.
- 57 R. Bauernschmitt and R. Ahlrichs, *Chem. Phys. Lett.*, 1996, **256**, 454–464.
- 58 G. Wang, M. Zhou, J. T. Goettel, G. J. Schrobilgen, J. Su, J. Li, T. Schloder and S. Riedel, *Nature*, 2014, **514**, 475–477.
- 59 D. Ciuparu, R. F. Klie, Y. M. Zhu and L. Pfeifferle, *J. Phys. Chem. B*, 2004, **108**, 3967–3969.